

Article

Methanol Oxidation on Graphenic-Supported Platinum Catalysts

Gladys Arteaga, Luis M. Rivera-Gavidia, Stephanie J. Martínez, Rubén Rizo , Elena Pastor * and Gonzalo García * 

Área de Química Física, Departamento de Química, Facultad de Ciencias, Universidad de La Laguna (ULL), Instituto de Materiales y Nanotecnología (IMN), 38200 La Laguna, Tenerife, Spain;

alu0100846713@ull.edu.es (G.A.); mlriviera@gmail.com (L.M.R.-G.);

sthephanie94@hotmail.com (S.J.M.); rjrizo57@gmail.com (R.R.)

* Correspondence: epastor@ull.edu.es (E.P.); ggarcia@ull.edu.es (G.G.);

Tel.: +34-922-318-071 (E.P.); +34-922-318-032 (G.G.)

Received: 19 November 2018; Accepted: 29 December 2018; Published: 6 January 2019



Abstract: Graphene oxide (GO), reduced graphene oxide by thermal treatment (rGO-TT), nitrogen-modified rGO (N-rGO), and carbon Vulcan were synthesized and employed in the current work as catalyst support for Pt nanoparticles, to study their properties and impact toward the methanol oxidation reaction (MOR) in sulfuric acid medium. Several physicochemical techniques, such as X-ray photoelectron spectroscopy (XPS), X-ray powder diffraction (XRD), Transmission electron microscopy (TEM), energy-dispersive X-ray spectroscopy (EDX), Raman, and elemental analysis were employed to characterize the novel materials, while potentiodynamic and potentiostatic methods were used to study catalytic performance toward the methanol oxidation reaction in acidic medium. The main results indicate a high influence of the support on the surface electronic state of the catalyst, and consequently the catalytic performance toward the MOR is modified. Accordingly, Pt/N-rGO and Pt/rGO-TT show the lowest and the highest catalytic performance toward the MOR, respectively.

Keywords: electrocatalysis; catalysts; methanol oxidation reaction; graphene; DMFC; Pt

1. Introduction

The search for alternatives to the use of fossil fuels, and the study and development of new green technologies for energy supply is an imperative necessity in order to fight global warming. Direct methanol fuel cells (DMFC) are an example of these energy-conversion devices [1–8]. They are able to supply energy from the electro-oxidation of a cheap resource like methanol, resulting not only in the reduction of release of harmful emissions, but also in the supply of high energy densities at low temperatures. The design of the catalysts to be used in DMFC systems is of outstanding importance. Many studies have confirmed that platinum is the most active metal when employed as a catalyst for the methanol oxidation reaction (MOR) [9–11].

However, the scarcity of this metal in the world and its high cost hinder the commercialization of such systems. In order to reduce as much as possible the amount of the catalytic material, the synthesis of Pt nanoparticles with high surface area/volume ratios, as well as the use of catalyst supports for a good dispersion of the metallic nanoparticles, is essential [12–14]. Furthermore, a high electrical conductivity of the catalyst support is the key factor for electrochemical reactions like the MOR. In this sense, graphene has emerged as a new-generation catalyst support, because of its excellent electrical conductivity and high surface area [15–18]. Many works have described chemical exfoliation methods of graphite to obtain so-called graphene oxide (GO) as a catalyst support. However, the conductivity

of such materials is lower than the highly desirable two-dimensional graphene, because of the high amount of oxygen groups on the surface. To fulfill conductivity problems, a great diversity of physical and chemical methods have been described in the literature for GO reduction to obtain reduced GO (rGO), with higher conductivity than GO itself [15–18]. On the other hand, it has been demonstrated that the surface chemistry of the catalytic support plays an essential role in the activity of the catalyst toward the MOR [19–23]. For example, the modification of carbon materials with heteroatoms, like nitrogen or sulfur, causes an electronic modulation of the carbonaceous lattice, resulting in a change in the electrocatalytic properties toward the MOR and other reactions of interest [15,18,23–25].

In the present paper, the synthesis of reduced graphene oxide (rGO) by a thermal treatment (rGO-TT) and nitrogen-modified rGO by the caffeine route (N-rGO) is reported, both of which are employed as supports for Pt nanoparticles. A deep physicochemical characterization of the novel catalysts was performed, and their catalytic performance toward the MOR was studied and compared with that of Vulcan XC72R supported Pt catalyst (Pt/C).

2. Materials and Methods

Sulfuric acid (p.a.; Merck, Darmstadt, Germany), methanol (p.a.; Merck, Darmstadt, Germany), potassium permanganate (>99.8%; Sigma-Aldrich, Saint Louis, MO, USA), caffeine (>99%; Sigma-Aldrich, Saint Louis, MO, USA), Vulcan XC-72R (Cabot, Boston, MA, USA), graphite (>99.8%; Sigma-Aldrich, Saint Louis, MO, USA), hydrogen peroxide (30% *v/v*; Foret, Barcelona, Spain), hydrogen (5% H₂/95% N₂; Air Liquide, Tenerife, Spain), (8 wt % H₂PtCl₆·6H₂O, Sigma-Aldrich, Saint Louis, MO, USA), Nafion solution (5 wt %; Sigma-Aldrich, Saint Louis, MO, USA), Ar (99.999%, Air Liquide, Tenerife, Spain), CO (99.997%, Air Liquide, Tenerife, Spain), and water (18.2 M Ω·cm⁻¹; Milli-Q, Millipore, Burlington, VT, USA) were purchased and then used for the synthesis of the graphene-based materials and the preparation of electrolyte solutions.

2.1. Synthesis of Graphene Oxide

Graphene oxide (GO) was prepared by following a modified Hummers method [15]. Briefly, 1 g of the graphite powder was mixed with 30 mL of concentrated H₂SO₄ cooled in an ice bath. Then, 3.5 g of KMnO₄ are slowly added while being stirred and cooled continuously. After removal from the ice bath, the mixture was diluted with Milli-Q water under stirring for 1 h at 35 °C. Then, the solution was heated up to 95–98 °C over 30 min. Next, 200 mL of ultrapure water was gradually introduced, followed by 1.25 mL of 30% *v/v* H₂O₂, and stirring was maintained for 30 min. Finally, the dispersion was centrifuged with Milli-Q water, until a pH of 7 was achieved in the supernatant liquid. The material was dried using an oven at 60 °C overnight.

2.2. Synthesis of Reduced Graphene Oxide Materials

In order to produce N-rGO, an adequate amount (4 mmol) of reducing agent (caffeine) was ultrasonically dispersed in Milli-Q water and mixed with a GO aqueous dispersion (0.015 g mL⁻¹). The final dispersion was placed into a Teflon-lined autoclave and heated at 160 °C for 10 h. Then, N-rGO was washed by centrifugation, employing Milli-Q water, and transferred to an oven at 60 °C for 24 h.

The rGO-TT was obtained by reduction of GO through a heat treatment under a reductive atmosphere (5% H₂/95% N₂ at 100 mL/min) in a tubular furnace. The thermal treatment comprised a ramp temperature of 5 °C/min from room temperature, up to 200 °C. This temperature was maintained for 30 min; finally, a ramp temperature of 5 °C/min was applied up to 450 °C where it was preserved for 1 h.

2.3. Synthesis of Pt/C, Pt/N-rGO, and Pt/rGO Catalysts

Platinum nanoparticles supported on carbon black Vulcan XC-72R, N-rGO, and rGO-TT were synthesized following the formic acid method [6]. Briefly, catalyst support was dispersed in 2 M

formic acid solution under sonication. Then, the mixture was heated at 80 °C under stirring, and an appropriate amount of metal precursor (H_2PtCl_6) was employed to obtain theoretical platinum loading of 20 wt % in the catalyst. The suspension was filtered, washed with ultrapure water, and dried at 60 °C overnight.

2.4. Physicochemical Characterization

Powder XRD spectra were acquired from X'Pert PRO X-ray diffractometer (PANalytical, Madrid, Spain) to determine the crystal structure. $\text{CuK}\alpha$ radiation ($\lambda = 1.5405 \text{ \AA}$) was employed, and 2θ data were collected from 20° to 100° with a scanning rate of 0.04 s^{-1} . Crystalline phases were identified by comparing the experimental diffraction patterns with the Joint Committee on Powder Diffraction Standards (JCPDS).

Elemental analysis with an experimental error close to 0.04% was performed using an Elemental Analyzer CNHS FLASH EA 1112 (Thermo Scientific, Madrid, Spain).

Raman spectra were collected employing a RENISHAW confocal Raman microscope, model inVia (RENISHAW, Gloucestershire, United Kingdom), with a green laser ($\lambda = 532 \text{ nm}$) in the 100 to 3200 cm^{-1} range.

Transmission electron microscopy (TEM) images were obtained from a HRTEM JEOL JEM 2100 operating (JEOL Ltd., Tokyo, Japan) at 200 eV. Obtained images were used to evaluate the morphology and agglomeration degree, as well as to calculate the average Pt nanoparticle sizes.

Chemical composition of the catalysts was determined by energy dispersive X-ray analysis (EDX, Oxford 6699 ATW, Oxford, Oxfordshire, UK), and X-ray photoelectron spectroscopy (XPS) data were obtained with a SPECS GmbH customized system (SPECSTM, Berlin, Germany) for surface analysis, equipped with a non-monochromatic X-ray source XR 50 and a hemispherical energy analyzer (PHOIBOS 1509MCD). Photoelectrons were excited by using $\text{MgK}\alpha$ line (1253.6 eV) operating at 200 W/12 kV. Powder samples were attached onto Cu foil and were placed first in the pre-treatment chamber at room temperature for several hours, before being transferred to the analysis chamber. The XPS data were signal averaged for a large enough number of scans to get a good signal/noise ratio, at increments of 0.1 eV and fixed pass energy of 25 eV. High-resolution spectra envelopes were obtained by curve fitting synthetic peak components, using the software XPSpeak. The raw data were used with no preliminary smoothing. Symmetric Gaussian—Lorentzian product functions were employed to approximate the line shapes of the fitting components. Binding energies were calibrated relative to the C 1s peak from the graphitic carbon at 284.6 eV.

2.5. Electrochemical Characterization

All electrochemical experiments were carried out at room temperature using a three-electrode glass cell, a carbon rod as a counter electrode and a reversible hydrogen electrode (RHE) as a reference electrode. All the potentials in this work were given against the RHE.

The working electrode consisted of a certain amount of the catalyst deposited as a thin layer over a glassy carbon disc (0.196 cm^2). The ink was prepared by mixing 2 mg of the catalyst powder, 15 μL of Nafion solution, and 500 μL of Milli-Q water.

Electrochemical measurements were performed with a PC-controlled Autolab PGSTAT30 potentiostat-galvanostat (Metrohm, Herisau, Switzerland) in 0.5 M H_2SO_4 electrolyte solution. A total of 2 M CH_3OH + 0.5 M H_2SO_4 solution was used to study the methanol oxidation reaction (MOR). Ar was employed to deoxygenate all solutions, as well as CO for CO stripping experiments. The last experiments were recorded at 0.02 V s^{-1} after bubbling CO through the cell for 10 min while keeping the electrode at 0.10 V, followed by Ar purging for 30 min to completely remove the excess CO. CO stripping voltammograms were recorded, by first scanning negatively until 0.05 V so that the entire hydrogen region was probed, and then scanning positively up to 1.2 V. Methanol cyclic voltammograms (CVs) were recorded between 0.05 and 1.0 V at a scan rate of 0.02 V s^{-1} , while current transients were obtained by stepping the potential from 0.05 V to the final oxidation potential

($0.50 < E_f < 0.90$ V). Tafel plots were calculated from stationary currents achieved at 300 s during the chronoamperometry experiments. Currents were normalized by the electroactive surface area (ESA) calculated from CO stripping experiments, by using a conversion factor of $240 \mu\text{C cm}^{-2}$ (12.6 cm^2 for Pt/C, 8.2 cm^2 for Pt/rGO-TT and 9.1 cm^2 for Pt/N-rGO).

3. Results and Discussion

3.1. Physicochemical Characterization

Figure 1 displays the X-ray diffractograms for graphite, carbon Vulcan, GO, rGO-TT, N-rGO, Pt/C, Pt/rGO-TT, and Pt/N-rGO. Graphite depicts a sharp diffraction peak at 24.6° , which is related to the (002) plane, and a small diffraction peak at 54° associated to the (004) facet [15]. The GO formation from the oxidation of graphite is detected by the broad diffraction peak at 10.7° , which is related to the (101) diffraction plane and by the absence of the diffraction peaks associated to graphite [15]. Additionally, Table 1 shows the expansion of the C–C interplanar spacing from 0.34 nm (graphite) to 0.82 nm (GO), due to the growth of oxygen functional groups between the graphitic layers [15].

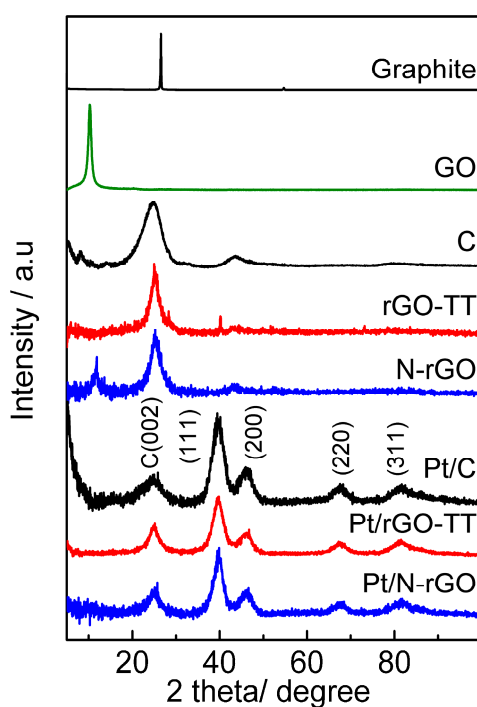


Figure 1. XRD patterns of graphite, graphene oxide (GO), Vulcan carbon (C), reduced graphene oxide by thermal treatment (rGO-TT), nitrogen-modified reduced graphene oxide (N-rGO), Pt/C, Pt/rGO-TT, and Pt/N-rGO.

Table 1. X-ray diffraction (XRD) parameters for all studied materials (d_{hkl} = interplanar spacing).

Catalyst	Position _{hkl} 2θ/°	d_{hkl} /nm	Number of Layers	Pt Crystallite Size/nm
Graphite	26.5 C(002)	0.34 C(002)	121	
GO	10.7 C(002)	0.82 C(002)	11	
Vulcan	24.7 C(002)	0.36 C(002)	6	-
rGO-TT	25.2 C(002)	0.35 C(002)	12	
N-rGO	25.3 C(002)	0.35 C(002)	9	
Pt/C	67.4 Pt(220)	0.23 Pt(111)	-	2.3
Pt/rGO-TT	67.5 Pt(220)	0.23 Pt(111)	-	2.4
Pt/N-rGO	67.6 Pt(220)	0.23 Pt(111)	-	2.0

On the other hand, Vulcan carbon, rGO-TT, and N-rGO reveal similar interplanar spacing (Table 1) and X-ray patterns (Figure 1), which indicate the restoration of the graphite C–C lattice and the elimination of oxygen functional groups between the graphitic layers in rGO materials. Also, a small diffraction peak at ca. 45° associated to the (100) plane is observed at the three carbon supports. The number of graphene layers that was estimated from the Debye–Scherrer equation and the Bragg law is also included in Table 1. The success of GO, rGO-TT, and N-rGO formation can be easily perceived by the diminution of the graphene layers in comparison to graphite. In this context, a graphite behavior was suggested for materials with more than 12 graphene layers, and therefore, a graphenic-like behavior is expected for all materials of the current work [26]. On the other hand, it is also important to note that N-rGO reveals a small diffraction peak at 10.7° associated to GO, which suggests a partial reduction of GO when caffeine is employed as a reducing agent [15].

Additionally, Figure 1 depicts X-ray diffractograms of Pt/C, Pt/rGO-TT, and Pt/N-rGO, in which the typical face centered cubic (*fcc*) structure of Pt is discerned at $2\theta = 40^\circ, 46^\circ, 68^\circ,$ and 82° , associated to the subsequent planes: (111), (200), (220), and (311) (JPCDS 00-004-0802). It is remarkable that the absence of the diffraction peak is at 10.7° for Pt/N-rGO, which suggests a reduction of the oxygen functional groups by the formic acid that is employed to reduce the metal precursor. In addition, it is important to highlight the absence of Pt crystalline oxides at all catalysts. However, the presence of Pt amorphous oxides should not be ruled out, since the oxygen content in graphenic-based materials is high (see Table 2). The most important crystallographic parameters of Pt-based catalysts are depicted in Table 1, in which similar interplanar spacing for all catalysts, smaller crystallite size for Pt/N-rGO than Pt/C and Pt/rGO-TT, and a small but visible lattice contraction in graphenic-based catalysts are discerned.

Table 2. Composition acquired by energy dispersive X-ray analysis (EDX) analysis and * elemental analysis for all studied materials.

Composition (% Weight)			
Material	C	O	N *
Graphite	80.0	20.0	
Carbon	96.5	3.5	-
GO	48.0	52.0	-
rGO-TT	75.3	24.7	-
N-rGO	73.0	21.0	6.0
Pt/C	96.4	3.6	-
Pt/rGO-TT	86.9	13.1	-
Pt/N-rGO	78.3	15.7	6.0

Scanning electron spectroscopy (SEM) coupled with energy dispersive X-ray spectroscopy (EDX) was employed to study the morphology, distribution, surface topography, and semi-quantitative bulk composition of the catalysts. The amount of Pt incorporated into each sample was close to the nominal value (19.0 ± 1.5 wt %). Figure 2 displays SEM images in the microscale for all materials synthesized. Pt/C reveals a smooth and homogeneous surface, while a granular and porous structure is observed at Pt/rGO-TT and Pt/N-rGO.

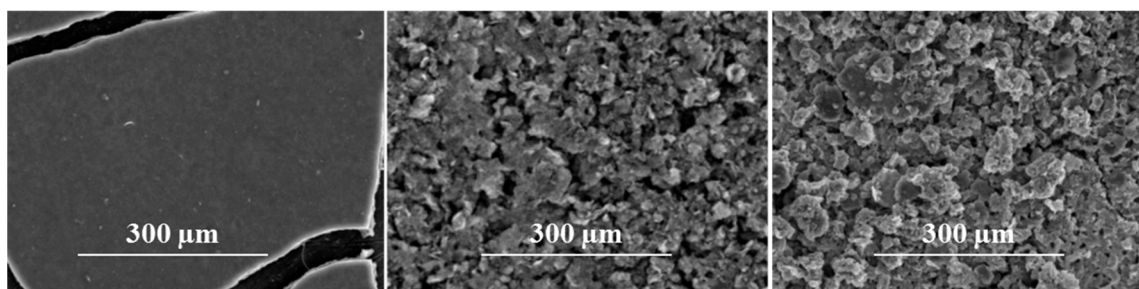


Figure 2. Scanning electronic microscopy (SEM) images for Pt/C (left panel), Pt/rGO-TT (middle panel), and Pt/N-rGO (right panel).

Table 2 discloses a strong increment of the oxygen content after GO production, which is reduced in the first stage after rGO-TT and N-rGO formation, and in the second stage after Pt deposition. The last stage is in agreement with the X-ray diffraction pattern of N-rGO, as the small peak associated with oxide species disappears after the addition of formic acid. It is noteworthy that even after Pt deposition, both graphenic catalysts show a higher amount of oxygen than carbon-supported Pt.

Raman spectroscopy (spectra are not shown) was employed to study the structural changes, the disorder degree, and the crystallographic size in the basal plane (L_a) of graphenic materials. With this end, the following equation was employed [27,28]:

$$L_a(\text{nm}) = \left(2.4 \times 10^{-10}\right) \cdot \lambda_l^4 \cdot \left(\frac{I_D}{I_G}\right)^{-1} \quad (1)$$

where λ_l is the excitation wavelength of the laser (532 nm), I_D is the peak intensity at 1360 cm^{-1} (associated to sp^3 carbon domains), and I_G is the peak intensity at 1580 cm^{-1} (related to sp^2 bonds into the graphitic grid). The main results indicate an increment of the disorder ($I_D/I_G \sim 0.9$) compared to graphite ($I_D/I_G \sim 0.15$), and the similar $L_a \sim 20 \text{ nm}$ for Vulcan carbon and all graphenic materials. The latter is the expected result, since structural disorder by edges, finite size, and carbon hybridization by heteroatom–C bond formation is usually reported in this type of materials [15,18].

Morphology, particle size, and agglomeration degree were studied by transmission electron microscopy (TEM). Figure 3 shows TEM images of Pt/C, Pt/rGO-TT, and Pt/N-rGO catalysts. Meanwhile, Figures S1–S3 depict high-resolution TEM images for all electrocatalysts employed in the current work. Spherical Pt nanoparticles are homogeneously dispersed on carbon sheets; however, the agglomeration degree increases with the amount of oxygen in the catalyst in the subsequent way: Pt/C < Pt/rGO-TT < Pt/N-rGO. Therefore, Pt nanoparticles seem to nucleate and grow referentially at surface oxygenated sites. Regarding the particle sizes, Figure 3 includes histograms for each catalyst, and shows increments in the following way: Pt/ N-rGO ($3.14 \pm 0.50 \text{ nm}$) < Pt/C ($3.28 \pm 0.25 \text{ nm}$) < Pt/rGO-TT ($3.32 \pm 0.43 \text{ nm}$). The last is in agreement with the trend observed for the crystallite size values calculated by XRD, although the values are slightly lower than those achieved by TEM, which is expected (i.e., crystallite size \leq grain size \leq particle size).

X-ray photoelectron spectroscopy (XPS) was carried out to identify and quantify the surface composition and the chemical state of the elements (see Table 3). Deconvoluted spectra for Pt, C, O, and N are presented in Figures 4 and 5. The Pt 4f signal (Figure 4) is resolved into three doublets in all electrocatalysts. The most intense Pt $4f_{7/2}$ component at lower binding energy is attributed to metallic Pt⁰, while the second doublet is assigned to Pt²⁺, and the third doublet at higher binding energy is related to the higher oxidation state of Pt⁴⁺. According to Table 3, there is a peak shift of metallic Pt to a lower binding energy for graphenic-based supports. The latter indicates a charge transfer from graphenic-based supports to platinum. However, Pt²⁺ species (i.e., PtO) increase to the detriment of metallic Pt at Pt/N-rGO material.

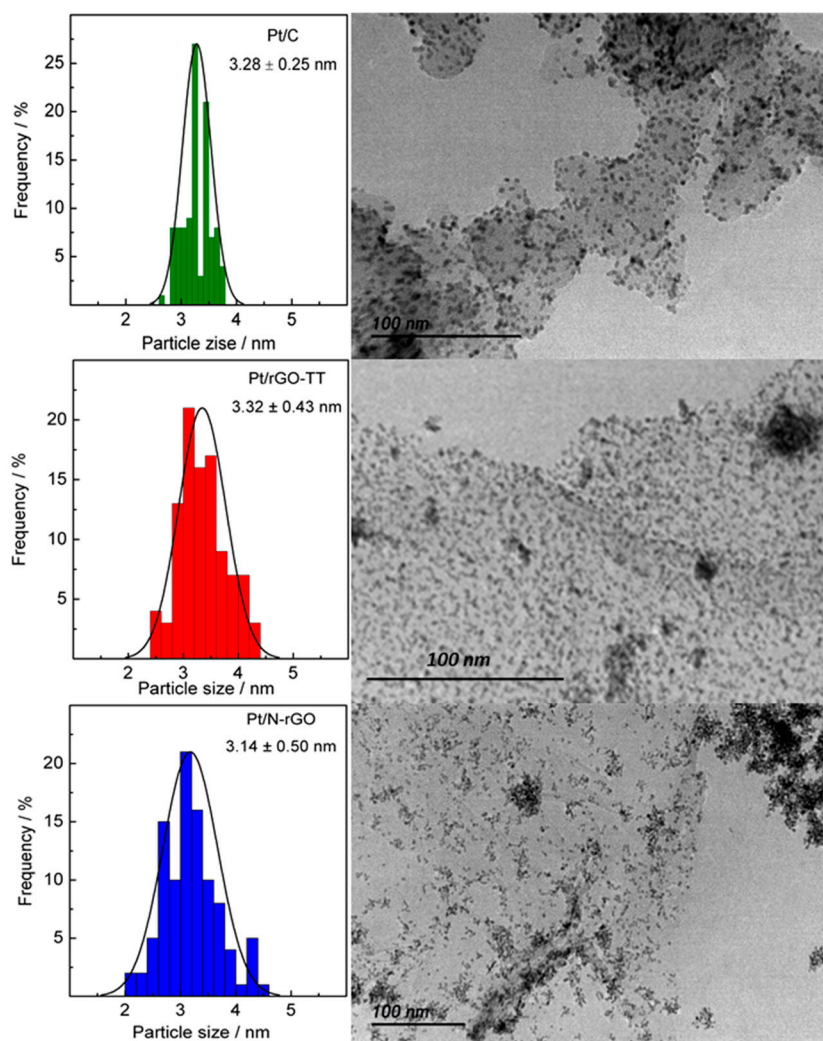


Figure 3. Transmission electron micrographs and particle size distribution histograms of the catalysts.

Table 3. X-ray photoelectron spectroscopy (XPS) analysis of the catalysts.

Elements	Pt4f	C1s	O1s	
Catalysts				
Pt/C	Pt ⁰	71.5 (62)	C-C 284.6 (81)	Pt oxides 530 (5)
	Pt ²⁺	72.4 (31)	C-N -	O=C 531.1 (10)
	Pt ⁴⁺	73.5 (7)	C-OH 285.8 (14)	OH-C 532.8 (72)
			C=O 287 (4)	O-C=O 534.1 (13)
			O-C=O 289.1 (1)	H ₂ O - 530 (3)
Pt/rGO-TT	Pt ⁰	71.2 (63)	C-C 284.6 (68)	Pt oxides 530 (3)

Table 3. Cont.

Elements	Pt4f	C1s	O1s					
Catalysts								
Pt/rGO-TT	Pt ²⁺	72.3 (30)	C-N	-	O=C	531.2 (23)		
	Pt ⁴⁺	74.3 (7)	C-OH	285.8 (15)	OH-C	532.9 (58)		
			C=O	287 (10)	O-C=O	533.9 (9)		
			O-C=O	288.7 (7)	H ₂ O	535.2 (7)		
Pt ⁰	71.2 (49)	C-C	284.5 (52)	Pt oxides	530.1 (4)			
Pt/N-rGO	Pt ²⁺	72.1 (42)	C-N	285.3 (14)	O=C	531.2 (33)	N1s	
	Pt ⁴⁺	74.0 (10)	C-OH	285.9 (12)	OH-C	532.7 (48)	Pyridinic	398.7 (29)
			C=O	287.1 (12)	O-C=O	534 (12)	Pyrrolic	400.2 (49)
			O-C=O	288.5 (10)	H ₂ O	535 (2)	Quaternary	401.2 (22)
			$\pi-\pi^*$	290.0 (2)	-	-	-	-

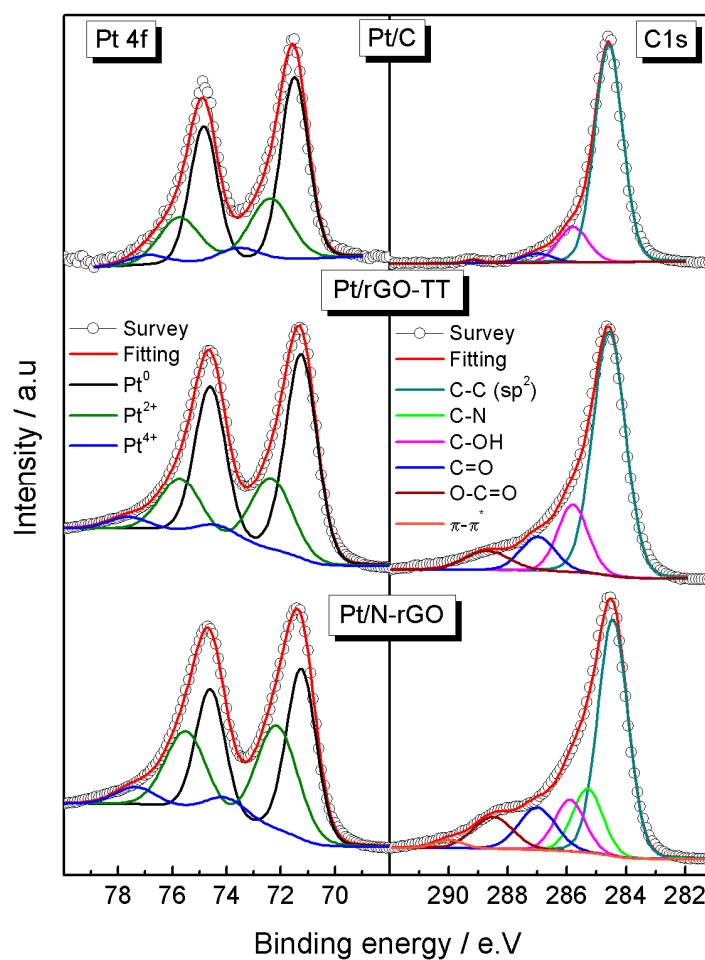


Figure 4. Pt 4f (left panels) and C1s (right panels) XPS spectra of the catalysts.

The C1s signal provides detailed information about the presence of oxygen and nitrogen species bonded to carbon atoms (Figure 4). As can be seen, the carbon signal is mainly composed by graphitic carbon (C1), followed by different oxygenated species at higher binding energy values, such as C–OH (C3), C=O (C4), and carboxylic bonds (C5) [29]. In addition to these signals, Pt/NrGO reveals an additional component at ca. 285.3 (C2) ascribed to nitrogen species bonded to carbon atoms. Indeed, the strong N1s signal (Figure 5) confirms that the last statement since the nitrogen species, such as pyridinic, pyrrolic, and N-quaternary, are clearly identified. Also, a small but visible signal at ca. 289 eV ascribed to a π - π^* shakeup satellite for Pt/Vulcan and Pt/NrGO catalysts is observed [30].

Interestingly, the O1s signal (Figure 5) reveals different surface oxygenated species, which strongly depend on the substrate. In agreement with the C1s signal, C=O (O2:~531.05 \pm 0.05 eV) and C–OH (O3:~533.5 \pm 0.5 eV) species are the main components for all materials [29]. Signals related to carboxyl groups (O4) and platinum oxides (O1) appear in minor proportion, while intercalated water (O5) is only perceived at graphenic materials. On the other hand, Pt/NrGO shows similar intensities for C–OH and C=O species, and the most intense component is associated to C–O species. All XPS information is summarized in Table 3.

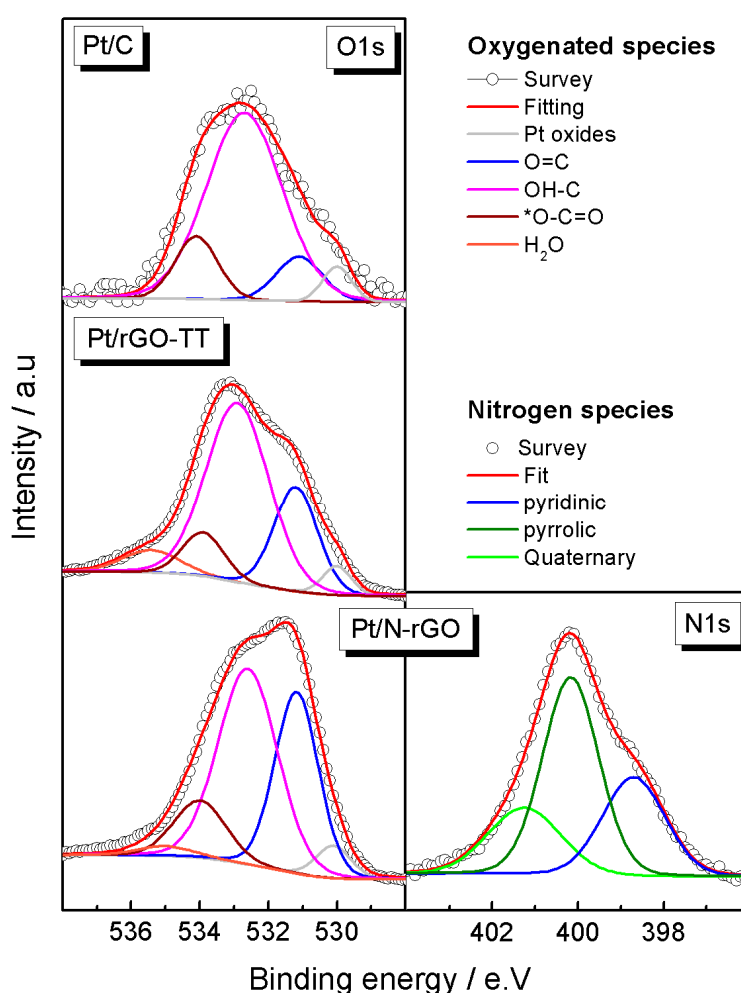


Figure 5. O1s (left panels) and N1s (right panel) XPS spectra of the catalysts.

3.2. Electrochemical Characterization

CO stripping experiments were performed to (i) characterize the catalyst surface; (ii) achieve catalytic activity towards CO oxidation, which is one of the most important catalyst poisons; and (iii) acquire the electroactive surface area (ESA). Figure 6 shows a similar CO oxidation peak value ($CO_p = 0.83$ V) for all catalysts. Noticeable, Pt/N-rGO reveals a broader CO oxidation peak, with an anodic tail that ends at 1.2 V. Additionally, the onset potential for the CO oxidation reaction is 0.70 V for Pt/rGO-TT, 0.72 V for Pt/C, and 0.75 V for Pt/N-rGO. These parameters indicate a higher CO tolerance for Pt/rGO-TT than for Pt/C, and the even lower one for Pt/N-rGO. Also, an increase of the double-layer capacitive current is observed at graphenic-based materials, especially relevant for Pt/N-rGO. The latter results and the low catalytic activity towards the CO oxidation on Pt/N-rGO may be ascribed to the high amount of surface-oxygenated species, i.e., PtO and PtO₂. Regarding the ESA, the values increase in the following way: Pt/rGO-TT (8.2 cm²) < Pt/N-rGO (9.1 cm²) < Pt/C (12.6 cm²). The last is in agreement with TEM analysis, in which high Pt agglomeration degree was detected at graphenic-based catalysts.

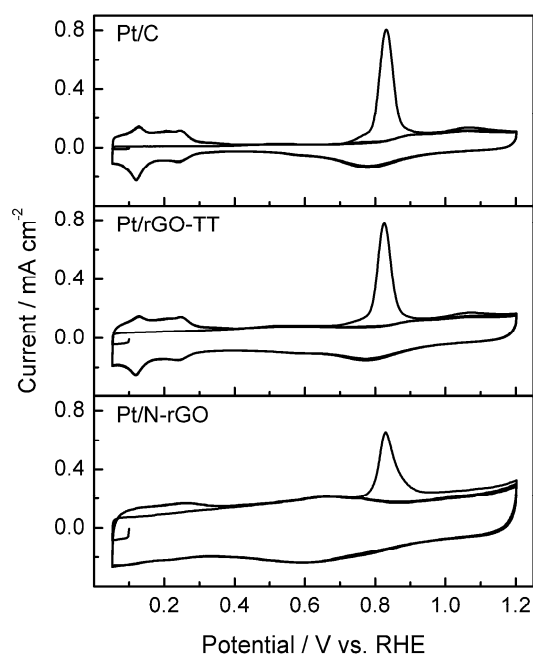


Figure 6. CO stripping voltammograms recorded at Pt/C, Pt/rGO-TT, and Pt/N-rGO catalysts in 0.5 M H₂SO₄. $E_{ad} = 0.1$ V; scan rate = 0.02 V s⁻¹.

The catalytic performance toward the methanol oxidation reaction (MOR) was evaluated by potentiodynamic (Figure 7) and potentiostatic (Figure 8) experiments. Figure 7 shows the lowest performance for Pt/N-rGO toward the MOR, which is in disagreement with what has been reported by other authors [31,32]. This different catalytic performance may be ascribed to the elevated amount of Pt surface oxide species (PtO and PtO₂ observed by XPS analysis) by using the caffeine route for the synthesis of the N-rGO, which inhibits the methanol adsorption step (see below).

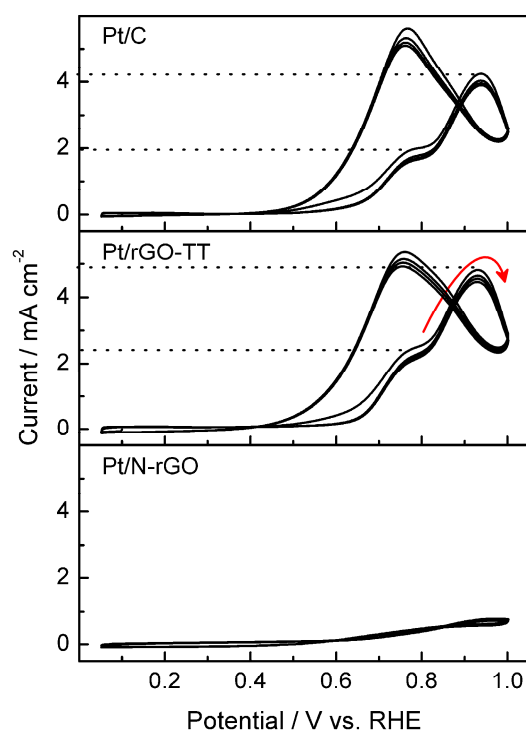


Figure 7. Methanol oxidation recorded for Pt/C, Pt/rGO-TT, and Pt/N-rGO catalysts in 2 M CH₃OH + 0.5 M H₂SO₄. Scan rate = 0.02 V s⁻¹.

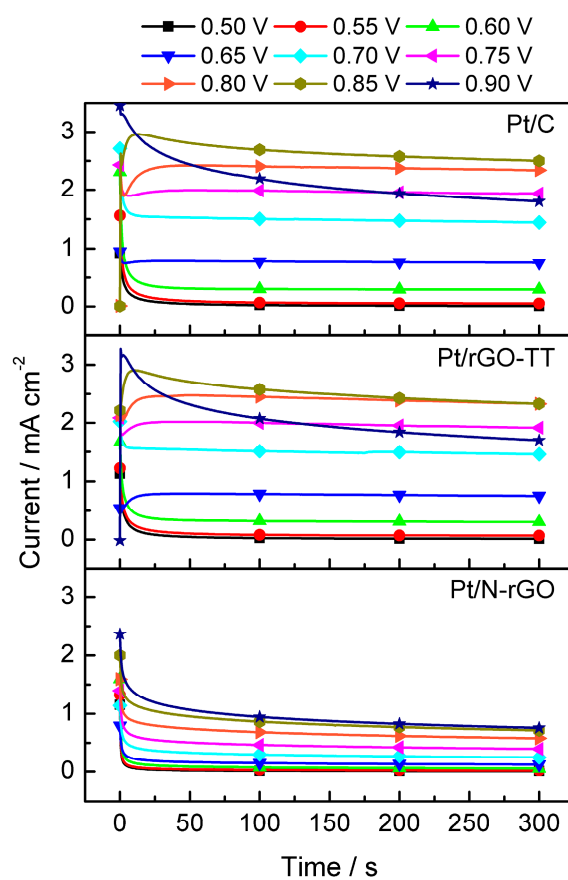


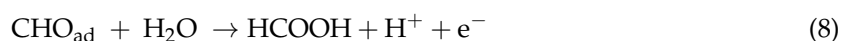
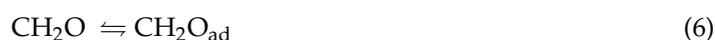
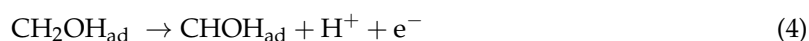
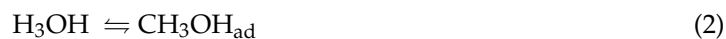
Figure 8. Current transients for methanol oxidation on Pt/C, Pt/rGO-TT, and Pt/N-rGO catalysts in 2 M CH₃OH + 0.5 M H₂SO₄. $E_i = 0.05$ V, 0.50 V $\leq E_f \leq 0.90$ V.

Additionally, similar voltammetric profiles with comparable onset potentials (~ 0.5 V) and analogous anodic ($E_{Pa} \sim 0.93$ V) and cathodic ($E_{Pc} \sim 0.76$ V) peak potentials are observed for Pt/rGO-TT and Pt/C. However, a close inspection of Figure 7 reveals higher anodic currents at Pt/rGO-TT than Pt/C during the positive sweep potential. Indeed, the pre-peak at ca. 0.77 V reveals higher current density at Pt/rGO-TT (2.4 mA cm^{-2}) than at Pt/C (2.0 mA cm^{-2}). The current peak during the anodic sweep (j_{Pa}) is 4.9 mA cm^{-2} at Pt/rGO-TT and 4.2 mA cm^{-2} at Pt/C, while the current peak during the cathodic sweep (j_{Pc}) is 5.4 mA cm^{-2} at Pt/rGO-TT and 5.6 mA cm^{-2} at Pt/C. The j_{Pa}/j_{Pc} ratio is usually employed to estimate the tolerance of the catalyst to adsorbed reaction intermediates (mainly CO_{ad}). Pt/C shows the lowest j_{Pa}/j_{Pc} value and appears as the catalyst with the highest tolerance, which is not in agreement with the CO stripping experiments in Figure 6. However, a recent work states that the j_{Pc} is not related to a residual intermediate of the MOR, and the j_{Pa}/j_{Pc} ratio is associated with the oxophilicity degree of the catalyst [33]. Thus, higher j_{Pa}/j_{Pc} value indicates higher oxophilicity degree, and consequently, Pt/rGO-TT appears to be the material with the highest oxophilicity. The last is in agreement with the physicochemical characterization, as well as with the CO stripping experiments, in which Pt/rGO-TT reveals the highest CO tolerance.

Figure 7 depicts current transients achieved from an initial potential of 0.05 V, in which methanol does not oxidize, to a final potential ($0.50 \leq E \leq 0.90$ V) where the MOR takes place. In agreement with potentiodynamic experiments, Pt/N-rGO develops the lowest performance toward the MOR in all potential ranges studied. In the same way, Pt/rGO-TT and Pt/C reveal similar better performance toward the alcohol oxidation. Interestingly, Pt/rGO-TT and Pt/C develops inflection points at short times at the same potential range ($0.65 \leq E \leq 0.75$), where the onset potential for the CO removal (Figure 5) and the pre-peak at the potentiodynamic experiments in presence of methanol is observed (Figure 6). This result suggests a change of rate-determining step (RDS), which may be attributed to an enhancement of the water dissociation reaction (i.e., OH_{ad} formation) necessary to remove CO from the catalyst surface [34,35]. Additionally, it is observed that at $E \geq 0.85$ V (anodic peak during the positive sweep potential, Figure 6), the current decay is faster at Pt/rGO-TT and Pt/C, which is related to the low performance of Pt oxide surface toward the MOR [36].

Further characterization of the catalytic activity of the synthesized materials was carried out by a Tafel plot analysis. A Tafel slope is usually employed to determine the rate-determining step (RDS), and therefore, the reaction mechanism may be inferred from Tafel slope values. Figure 9 depicts a Tafel plot obtained from the current transients of methanol oxidation for the three catalysts (Figure 8) at different final potentials ($0.50 \leq E \leq 0.90$ V) in an acidic medium. Pt/C shows a Tafel slope of 120 mV dec^{-1} , while Pt/rGO-TT and Pt/C reveal a Tafel slope of 75 mV dec^{-1} . In order to clarify the operating reaction mechanism on the catalysts involved in the current work, the main steps for MOR are briefly described.

First there is the electrosorption and dehydrogenation of methanol onto a suitable surface. The complete electrosorption and dehydrogenation steps yield to adsorbed carbon monoxide (CO_{ad}), otherwise formaldehyde and formic acid may be produced [37]:



Second, there is the electrooxidation of CO_{ad} . Water dissociation on the catalyst surface (formation of adsorbed OH) is needed to perform the CO_{ad} oxidation to CO_2 , and consequently liberate the catalyst surface [31,38,39]:



A Tafel slope of 120 mV dec^{-1} suggests that the rate-determining step is related to the first electrochemical step, and therefore the rate of MOR at Pt/N-rGO is limited by the “electrosorption and dehydrogenation step”, i.e., Reaction 3. The latter is in complete agreement with the low current developed by the Pt/N-rGO materials during the MOR, and should be ascribed to a non-suitable surface for methanol dehydrogenation, which is comprised of strongly bonded oxygen species onto the surface, i.e., PtO and PtO₂ [36]. On the other hand, a Tafel slope close to 60 mV dec^{-1} (Pt/C and Pt/rGO-TT) indicates a chemical reaction after an electrochemical reaction as the RDS, i.e., the surface diffusion of CO_{ad} toward the active site (reaction 11). Both materials revealed similar catalytic performance toward the MOR, although a slight enhancement of the CO tolerance at Pt/rGO-TT was perceived. The last seems to be related to electronic effects (charge transfer from rGO-TT to Pt) and to a higher amount of C–OH species onto the graphenic-based catalyst (bifunctional effect).

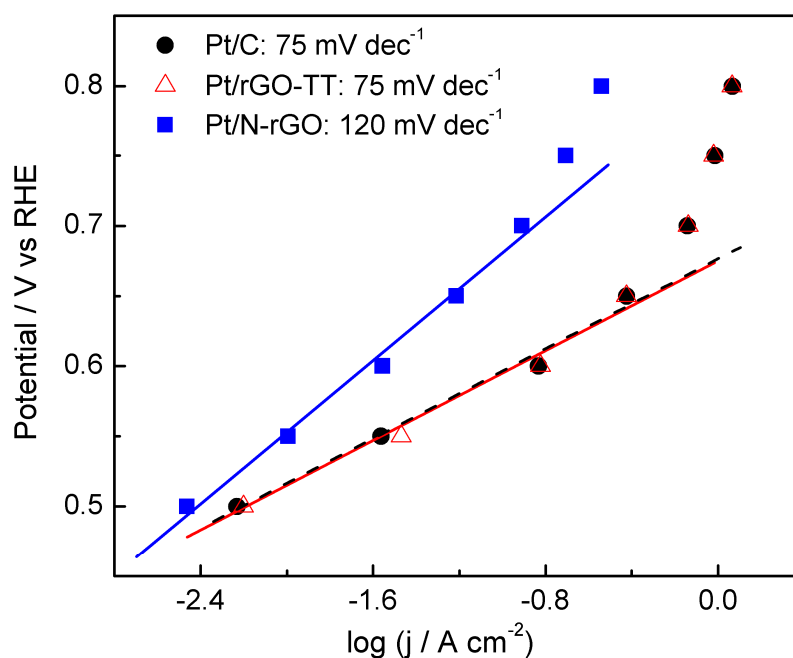


Figure 9. Tafel plots obtained at 300 s from Figure 8.

4. Conclusions

Graphene oxide (GO), reduced graphene oxide (rGO-TT), nitrogen-modified rGO (N-rGO), and carbon-supported Pt materials using these supports were successfully synthesized and fully characterized. Results have shown that the support conditions the state of oxidation of metal nanoparticles at the surface of the catalysts, which control the activity of a specific electrochemical reaction. Indeed, a small addition of nitrogen into the catalyst support induces a change of the rate-determining step from a chemical reaction after an electrochemical reaction to the first electron. Thus, Pt/N-rGO displays the worst performance toward the methanol oxidation reaction, while

Pt/rGO-TT not only enhances the catalytic activity toward the alcohol oxidation, but also toward the most important catalyst poison.

Supplementary Materials: The following are available online at <http://www.mdpi.com/2571-9637/2/1/2/s1>, Figure S1: TEM image for Pt/C electrocatalyst, Figure S2: TEM image for Pt/rGO-TT electrocatalyst, Figure S3: TEM image for Pt/N-rGO electrocatalyst.

Author Contributions: Data curation, G.A. and S.J.M.; Formal analysis, L.M.R.-G.; Writing – original draft, R.R.; Writing – review & editing, E.P. and G.G.

Acknowledgments: The Spanish Ministry of Economy and Competitiveness (MINECO) has supported this work under project ENE2017-83976-C2-2-R (co-funded by FEDER). L.M.R. thanks the ACIISI for his PhD fellowships. G.G. acknowledges the Viera y Clavijo program (ACIISI and ULL) for financial support.

Conflicts of Interest: The authors declare no conflict of interest.

References

1. Guillén-Villafuerte, O.; Guil-López, R.; Nieto, E.; García, G.; Rodríguez, J.L.; Pastor, E.; Fierro, J.L.G. Electrocatalytic Performance of Different Mo-Phases Obtained during the Preparation of Innovative Pt-MoC Catalysts for DMFC Anode. *Int. J. Hydrog. Energy* **2012**, *37*, 7171–7179. [[CrossRef](#)]
2. Li, M.; Adzic, R.R. Low-Platinum-Content Electrocatalysts for Methanol and Ethanol Electrooxidation. In *Lecture Notes in Energy*; Shao, M., Ed.; Springer: London, UK, 2013; Volume 9, pp. 1–25.
3. Pérez-Rodríguez, S.; Corengia, M.; García, G.; Zinola, C.F.; Lázaro, M.J.; Pastor, E. Gas Diffusion Electrodes for Methanol Electrooxidation Studied by a New DEMS Configuration: Influence of the Diffusion Layer. *Int. J. Hydrog. Energy* **2012**, *37*, 7141–7151. [[CrossRef](#)]
4. Huang, L.; Zhang, X.; Wang, Q.; Han, Y.; Fang, Y.; Dong, S. Shape-Control of Pt–Ru Nanocrystals: Tuning Surface Structure for Enhanced Electrocatalytic Methanol Oxidation. *J. Am. Chem. Soc.* **2018**, *140*, 1142–1147. [[CrossRef](#)] [[PubMed](#)]
5. Roca-Ayats, M.; García, G.; Peña, M.A.; Martínez-Huerta, M.V. Titanium Carbide and Carbonitride Electrocatalyst Supports: Modifying Pt-Ti Interface Properties by Electrochemical Potential Cycling. *J. Mater. Chem. A* **2014**, *2*, 18786–18790. [[CrossRef](#)]
6. Calderón, J.C.; García, G.; Querejeta, A.; Alcaide, F.; Calvillo, L.; Lázaro, M.J.; Rodríguez, J.L.; Pastor, E. Carbon Monoxide and Methanol Oxidations on Carbon Nanofibers Supported Pt-Ru Electrodes at Different Temperatures. *Electrochim. Acta* **2015**, *186*, 359–368. [[CrossRef](#)]
7. Flórez-Montaño, J.; García, G.; Rodríguez, J.L.; Pastor, E.; Cappellari, P.; Planes, G.A. On the Design of Pt Based Catalysts. Combining Porous Architecture with Surface Modification by Sn for Electrocatalytic Activity Enhancement. *J. Power Sources* **2015**, *282*, 34–44. [[CrossRef](#)]
8. Rizo, R.; García, G.; Pastor, E. Methanol Oxidation on Bimetallic Electrode Surfaces. In *Encyclopedia of Interfacial Chemistry: Surface Science and Electrochemistry*; Wandelt, K., Ed.; Elsevier: Amsterdam, The Netherlands, 2018; Volume 5, pp. 719–729.
9. Anitha, V.C.; Zazpe, R.; Krbal, M.; Yoo, J.; Sopha, H.; Prikryl, J.; Cha, G.; Slang, S.; Schmuki, P.; Macak, J.M. Anodic TiO₂ Nanotubes Decorated by Pt Nanoparticles Using ALD: An Efficient Electrocatalyst for Methanol Oxidation. *J. Catal.* **2018**, *365*, 86–93. [[CrossRef](#)]
10. Wasmus, S.; Küwer, A. Methanol Oxidation and Direct Methanol Fuel Cells: A Selective Review. *J. Electroanal. Chem.* **1999**, *461*, 14–31. [[CrossRef](#)]
11. Planes, G. a.; García, G.; Pastor, E. High Performance Mesoporous Pt Electrode for Methanol Electrooxidation. A DEMS Study. *Electrochem. Commun.* **2007**, *9*, 839–844. [[CrossRef](#)]
12. Martínez Huerta, M.V.; García, G. Fabrication of Electro-Catalytic Nano-Particles and Applications to Proton Exchange Membrane Fuel Cells. In *Micro & Nano-Engineering of Fuel Cells*; Leung, D.Y.C., Xuan, J., Eds.; Sustainable Energy Developments; CRC Press: London, UK, 2015; pp. 95–129.
13. Rizo, R.; Sebastián, D.; Rodríguez, J.L.; Lázaro, M.J.; Pastor, E. Influence of the Nature of the Carbon Support on the Activity of Pt/C Catalysts for Ethanol and Carbon Monoxide Oxidation. *J. Catal.* **2017**, *348*, 22–28. [[CrossRef](#)]

14. Rizo, R.; Arán-Ais, R.M.; Padgett, E.; Muller, D.A.; Lázaro, M.J.; Solla-Gullón, J.; Feliu, J.M.; Pastor, E.; Abruña, H.D. Pt-Richcore/Sn-Richsurface/Ptskin Nanocubes As Highly Active and Stable Electrocatalysts for the Ethanol Oxidation Reaction. *J. Am. Chem. Soc.* **2018**, *140*, 3791–3797. [[CrossRef](#)] [[PubMed](#)]
15. Rivera, L.M.; Fajardo, S.; Arévalo, M.D.C.; García, G.; Pastor, E. S- and N-Doped Graphene Nanomaterials for the Oxygen Reduction Reaction. *Catalysts* **2017**, *7*, 278. [[CrossRef](#)]
16. Zhu, Y.; Chen, G.; Zhong, Y.; Zhou, W.; Shao, Z. Rationally Designed Hierarchically Structured Tungsten Nitride and Nitrogen-Rich Graphene-Like Carbon Nanocomposite as Efficient Hydrogen Evolution Electrocatalyst. *Adv. Sci.* **2018**, *5*, 1700603. [[CrossRef](#)] [[PubMed](#)]
17. Liang, H.; Li, C.; Chen, T.; Cui, L.; Han, J.; Peng, Z.; Liu, J. Facile Preparation of Three-Dimensional Co 1-x S/Sulfur and Nitrogen-Codoped Graphene/Carbon Foam for Highly Efficient Oxygen Reduction Reaction. *J. Power Sources* **2018**, *378*, 699–706. [[CrossRef](#)]
18. Rivera, L.M.; García, G.; Pastor, E. Novel Graphene Materials for the Oxygen Reduction Reaction. *Curr. Opin. Electrochem.* **2018**, *9*, 233–239. [[CrossRef](#)]
19. Sun, M.; Liu, H.; Liu, Y.; Qu, J.; Li, J. Graphene-based transition metal oxide nanocomposites for the oxygen reduction reaction. *Nanoscale* **2015**, *7*, 1250–1269. [[CrossRef](#)] [[PubMed](#)]
20. Chen, D.; Feng, H.; Li, J. Graphene Oxide: Preparation, Functionalization, and Electrochemical Applications. *Chem. Rev.* **2012**, *112*, 6027–6053. [[CrossRef](#)] [[PubMed](#)]
21. Chen, D.; Tang, L.; Li, J. Graphene-based materials in electrochemistry. *Chem. Soc. Rev.* **2010**, *39*, 3157–3180. [[CrossRef](#)]
22. Chetty, R.; Kundu, S.; Xia, W.; Bron, M.; Schuhmann, W.; Chirila, V.; Brandl, W.; Reinecke, T.; Muhler, M. PtRu Nanoparticles Supported on Nitrogen-Doped Multiwalled Carbon Nanotubes as Catalyst for Methanol Electrooxidation. *Electrochim. Acta* **2009**, *54*, 4208–4215. [[CrossRef](#)]
23. Maiyalagan, T. Synthesis and Electro-Catalytic Activity of Methanol Oxidation on Nitrogen Containing Carbon Nanotubes Supported Pt Electrodes. *Appl. Catal. B Environ.* **2008**, *80*, 286–295. [[CrossRef](#)]
24. Sebastián, D.; Nieto-Monge, M.J.; Pérez-Rodríguez, S.; Pastor, E.; Lázaro, M.J. Nitrogen Doped Ordered Mesoporous Carbon as Support of PtRu Nanoparticles for Methanol Electro-Oxidation. *Energies* **2018**, *11*, 831. [[CrossRef](#)]
25. Antonietti, M.; Oschatz, M. The Concept of “Noble, Heteroatom-Doped Carbons,” Their Directed Synthesis by Electronic Band Control of Carbonization, and Applications in Catalysis and Energy Materials. *Adv. Mater.* **2018**, *30*, 1706836. [[CrossRef](#)] [[PubMed](#)]
26. Ambrosi, A.; Chua, C.K.; Latiff, N.M.; Loo, A.H.; Wong, C.H.A.; Eng, A.Y.S.; Bonanni, A.; Pumera, M. Graphene and Its Electrochemistry—An Update. *Chem. Soc. Rev.* **2016**, *45*, 2458–2493. [[CrossRef](#)] [[PubMed](#)]
27. Zickler, G.A.; Smarsly, B.; Gierlinger, N.; Peterlik, H.; Paris, O. A Reconsideration of the Relationship between the Crystallite Size La of Carbons Determined by X-Ray Diffraction and Raman Spectroscopy. *Carbon N. Y.* **2006**, *44*, 3239–3246. [[CrossRef](#)]
28. Caçado, L.G.; Takai, K.; Enoki, T.; Endo, M.; Kim, Y.A.; Mizusaki, H.; Jorio, A.; Coelho, L.N.; Magalhães-Paniago, R.; Pimenta, M.A. General Equation for the Determination of the Crystallite Size La of Nanographite by Raman Spectroscopy. *Appl. Phys. Lett.* **2006**, *88*, 163106. [[CrossRef](#)]
29. Wagner, C.; Riggs, W.M.; Davis, L.E.; Moulder, J.F.; Muilenberg, G.E. *Handbook of X-ray Photoelectron Spectroscopy*; Muilenberg, G.E., Ed.; Perkin-Elmer Corporation: Eden Prairie, MN, USA, 1979.
30. Ganguly, A.; Sharma, S.; Papakonstantinou, P.; Hamilton, J. Probing the Thermal Deoxygenation of Graphene Oxide Using High-Resolution In Situ X-Ray-Based Spectroscopies. *J. Phys. Chem. C* **2011**, *115*, 17009–17019. [[CrossRef](#)]
31. Liu, D.; Li, L.; You, T. Superior catalytic performances of platinum nanoparticles loaded nitrogen-doped graphene toward methanol oxidation and hydrogen evolution reaction. *J. Colloid Interface Sci.* **2017**, *487*, 330–335. [[CrossRef](#)]
32. Xiong, B.; Zhou, Y.; Zhao, Y.; Wang, J.; Chen, X.; O’Hayre, R.; Shao, Z. The use of nitrogen-doped graphene supporting Pt nanoparticles as a catalyst for methanol electrocatalytic oxidation. *Carbon N. Y.* **2013**, *52*, 181–192. [[CrossRef](#)]
33. Chung, D.Y.; Lee, K.J.; Sung, Y.E. Methanol Electro-Oxidation on the Pt Surface: Revisiting the Cyclic Voltammetry Interpretation. *J. Phys. Chem. C* **2016**, *120*, 9028–9035. [[CrossRef](#)]

34. García, G.; Koper, M.T.M. Carbon Monoxide Oxidation on Pt Single Crystal Electrodes: Understanding the Catalysis for Low Temperature Fuel Cells. *ChemPhysChem* **2011**, *12*, 2064–2072. [[CrossRef](#)]
35. García, G. Correlation between CO Oxidation and H Adsorption/Desorption on Pt Surfaces in a Wide pH Range: The Role of Alkali Cations. *ChemElectroChem* **2017**, *4*, 459–462. [[CrossRef](#)]
36. Iwasita, T. Electrocatalysis of Methanol Oxidation. *Electrochim. Acta* **2002**, *47*, 3663–3674. [[CrossRef](#)]
37. Guillén-Villafuerte, O.; García, G.; Guil-López, R.; Nieto, E.; Rodríguez, J.L.; Fierro, J.L.G.; Pastor, E. Carbon monoxide and methanol oxidations on Pt/X@MoO₃/C (X = Mo₂C, MoO₂, Mo⁰) electrodes at different temperatures. *J. Power Sources* **2013**, *231*, 163–172. [[CrossRef](#)]
38. Gisbert, R.; García, G.; Koper, M.T.M. Oxidation of carbon monoxide on poly-oriented and single-crystalline platinum electrodes over a wide range of pH. *Electrochim. Acta* **2011**, *56*, 2443–2449. [[CrossRef](#)]
39. Gilman, S. The Mechanism of Electrochemical Oxidation of Carbon Monoxide and Methanol on Platinum. II. The “Reactant-Pair” Mechanism for Electrochemical Oxidation of Carbon Monoxide and Methanol. *J. Phys. Chem.* **1964**, *68*, 70–80. [[CrossRef](#)]



© 2019 by the authors. Licensee MDPI, Basel, Switzerland. This article is an open access article distributed under the terms and conditions of the Creative Commons Attribution (CC BY) license (<http://creativecommons.org/licenses/by/4.0/>).